



Quantum control of an oscillator with a Kerr-cat qubit

Received: 30 July 2024

Accepted: 21 May 2025

Published online: 06 June 2025

Andy Z. Ding ^{1,7}, Benjamin L. Brock ^{1,7}, Alec Eickbusch ^{1,2}, Akshay Koottandavida ^{1,3}, Nicholas E. Frattini ^{1,4}, Rodrigo G. Cortiñas ^{1,2}, Vidul R. Joshi ^{1,5}, Stijn J. de Graaf ^{1,2}, Benjamin J. Chapman ^{1,5}, Suhas Ganjam ^{1,2}, Luigi Frunzio ¹, Robert J. Schoelkopf ¹ & Michel H. Devoret ^{1,6}

Check for updates

Bosonic codes offer a hardware-efficient strategy for quantum error correction by redundantly encoding quantum information in the large Hilbert space of a harmonic oscillator. However, experimental realizations of these codes are often limited by ancilla errors propagating to the encoded logical qubit during syndrome measurements. The Kerr-cat qubit has been proposed as an ancilla for these codes due to its theoretically-exponential noise bias, which would enable fault-tolerant error syndrome measurements, but the coupling required to perform these syndrome measurements has not yet been demonstrated. In this work, we experimentally realize driven parametric coupling of a Kerr-cat qubit to a high-quality-factor microwave cavity and demonstrate a gate set that would enable universal quantum control of the cavity. We measure the decoherence of the cavity in the presence of the Kerr-cat and discover excess dephasing due to heating of the Kerr-cat to excited states. By engineering frequency-selective dissipation to counteract this heating, we are able to eliminate this dephasing, thereby demonstrating a high on-off ratio of control. Our results pave the way toward using the Kerr-cat to fault-tolerantly measure error syndromes of bosonic codes.

A major obstacle to scaling up quantum computers is noise, which causes logical errors and prevents the reliable execution of quantum algorithms. Quantum error correction (QEC) provides a path toward fault-tolerance^{1–4}, but this typically comes at the cost of significant resource overhead, often requiring hundreds of physical qubits per logical qubit^{5–9}. Bosonic codes offer a hardware-efficient alternative to multi-qubit QEC codes by redundantly encoding quantum information in the large Hilbert space of a harmonic oscillator^{10–15}. These codes have been employed to achieve landmark experimental demonstrations, including beyond break-even QEC of quantum memories^{16–19} and fully-autonomous QEC protocols^{20–22}. However, these experiments rely on an ancilla qubit to control the oscillator and perform quantum error

correction, such that errors on the ancilla can propagate to the logical qubit, limiting its lifetime.

In circuit quantum electrodynamics^{23,24} these realizations of bosonic codes typically use a microwave cavity as the oscillator and a transmon as the ancilla. The two are coupled dispersively, and since this dispersive interaction is transparent to transmon phase-flip errors, these QEC protocols are usually only sensitive to transmon bit-flip errors. Although fault-tolerant error syndrome measurements have been experimentally demonstrated using a transmon ancilla²⁵, another approach to achieving fault-tolerance is to use a biased-noise qubit as an ancilla for bosonic codes²⁶. Ideally, the error channel of such an ancilla should be

¹Departments of Applied Physics and Physics, Yale University, New Haven, CT, USA. ²Present address: Google Quantum AI, Santa Barbara, CA, USA. ³Present address: AWS Center for Quantum Computing, Pasadena, CA, USA. ⁴Present address: Nord Quantique, Sherbrooke, QC, Canada. ⁵Present address: Microsoft Azure Quantum, Redmond, WA, USA. ⁶Present address: UC Santa Barbara, Department of Physics, Google Quantum AI, Santa Barbara, CA, USA. ⁷These authors contributed equally: Andy Z. Ding, Benjamin L. Brock. e-mail: zhenghao.ding@yale.edu; benjamin.brock@yale.edu; michel.devoret@yale.edu

dominated by phase flips, with a negligible rate of bit flips compared to other rates in the system.

The Kerr-cat qubit (KCQ) has the potential to be exactly such an ancilla due to its promise of an exponential noise bias²⁷. Recent experimental realizations of KCQs have reached a strong noise bias of about 1000^{28–30} (corresponding to a bit-flip lifetime of ~1 ms and phase-flip lifetime of ~1 μs), and although these are not as large as we expect from theory, there are many possible methods for further improvement^{31–36}. With a strong noise bias and fast single-qubit gates^{29,37}, the only remaining ingredient for using the KCQ as an ancilla for bosonic codes is a coherent entangling operation between the KCQ and an oscillator that enables the measurement of error syndromes, which to date has not been demonstrated.

In this work, we experimentally demonstrate a coherent parametrically-driven conditional displacement (CD) gate between a KCQ and a high-quality-factor microwave cavity, where the cavity is displaced in one of two directions depending on the state of the KCQ. Combined with single-qubit gates on the KCQ, this CD gate enables universal quantum control of the cavity³⁸. We use this CD gate to measure the decoherence of the cavity in the presence of the KCQ and discover excess cavity dephasing due to heating of the KCQ into excited states, an effect that was not previously predicted. However, by engineering frequency-selective dissipation to counteract this heating³¹, we are able to eliminate this dephasing up to the precision of our measurements. This lack of dephasing indicates that the two systems do not entangle unless we are actively driving their interaction, demonstrating a high on-off ratio of control. Our results pave the way toward using the Kerr-cat as an ancilla for fault-tolerant syndrome measurements of bosonic codes²⁶, in particular the Gottesman-Kitaev-Preskill code¹¹ whose error syndromes can be mapped to an ancilla via CD gates^{39–41}.

Results

The KCQ consists of the degenerate ground state manifold of the Hamiltonian

$$H_{\text{KCQ}}/\hbar = -Ka^{\dagger 2}a^2 + \epsilon_2 a^{\dagger 2} + \epsilon_2^* a^2, \quad (1)$$

where a is the annihilation operator of the Kerr-oscillator mode, K is the Kerr nonlinearity of the mode, and ϵ_2 is the strength of the squeezing drive. This computational subspace is spanned by the orthonormal even- and odd-parity cat states $|\mathcal{C}_\alpha^\pm\rangle = \mathcal{N}_\alpha^\pm (|+\alpha\rangle \pm |-\alpha\rangle)$ (with normalization $\mathcal{N}_\alpha^\pm = 1/\sqrt{2(1 \pm e^{-2\alpha^2})}$)²⁷, where $\alpha = \sqrt{\epsilon_2/K}$ is assumed to be real without loss of generality. This gives rise to the Bloch sphere depicted in Fig. 1a. These cat states $|\mathcal{C}_\alpha^\pm\rangle$ form the X basis of the KCQ, while the parity-less cats $|\mathcal{C}_\alpha^{\pm i}\rangle = \mathcal{N}_\alpha^\pm (|+\alpha\rangle \pm i|-\alpha\rangle)$ form the Y basis. The Z basis consists of the even and odd superpositions of $|\mathcal{C}_\alpha^\pm\rangle$, which are approximately equal to the coherent states $|\pm\alpha\rangle$ for large α . The noise bias of the KCQ comes from the metapotential associated with H_{KCQ} ^{26,42}: it has a double-well structure with two global minima (corresponding to the coherent states) separated by a potential barrier³⁷. Dephasing of the Kerr-oscillator causes tunneling events between the wells, corresponding to bit-flip errors, which are exponentially suppressed by a factor $2\alpha^2 \exp(-2\alpha^2)$ due to the height of the potential barrier³³. On the other hand, photon-loss events in the Kerr-oscillator cause the cat states to change parity, corresponding to phase-flip errors, which are linearly amplified by a factor $2\alpha^2$ due to the average number of photons in the coherent states^{13,27,28,37}.

Following previous demonstrations^{28,29,33,37}, we experimentally realize the KCQ by squeezing a capacitively-shunted Superconducting Nonlinear Asymmetric Inductive eElement (SNAIL)^{43–45}. The SNAIL is a flux-tunable circuit described by the Hamiltonian $H_{\text{SNAIL}}/\hbar = \omega_a(\Phi_{\text{ext}})a^\dagger a + g_3(\Phi_{\text{ext}})(a + a^\dagger)^3 + g_4(\Phi_{\text{ext}})(a + a^\dagger)^4$, where g_3 and g_4 are the third and fourth order nonlinearities of the SNAIL, and Φ_{ext} is the external flux threading the SNAIL. The KCQ Hamiltonian in

Eq. (1) is obtained as the static effective Hamiltonian of the system when we apply a squeezing drive to the SNAIL at frequency $\omega_s = 2\omega_a$. A continuous $\sigma_z(\theta)$ rotation of the KCQ is realized by driving the SNAIL at its resonant frequency $\omega_s/2 = \omega_a$, while a discrete $\sigma_x(\pi/2)$ rotation is realized by turning off the squeezing drive and allowing the SNAIL mode to evolve under its bare Kerr-nonlinear Hamiltonian for time $T_K = \pi/K$ ^{37,46}. Together, these rotations enable universal single-qubit gates on the KCQ. To read out the logical information stored in this qubit, we use a process called cat-qubit readout (CQR)³⁷, which involves parametrically driving a beam-splitter interaction between the SNAIL circuit and a readout cavity (frequency ω_r and mode operator r) at the difference frequency $\omega_r - \omega_s/2$ while stabilizing the KCQ. After projecting the Hamiltonian of this interaction onto the computational basis of the KCQ, it takes the form of a conditional displacement of the readout cavity $H_{\text{CQR}} = g_{\text{CQR}}(r + r^\dagger)\sigma_z$ ³⁷, such that measuring the phase of the radiation leaking out of the readout cavity constitutes a readout of the KCQ along its Z axis.

The same conditional displacement interaction can be activated between the KCQ and a high-Q storage cavity (frequency ω_b and mode operator b) by driving the SNAIL at the difference frequency $\omega_b - \omega_s/2$. For clarity, we reserve the acronym CD for the conditional displacement interaction between the KCQ and the high-Q cavity. While driving this beamsplitter interaction at a rate g_{BS} , the static effective Hamiltonian of the system in the rotating frame of the SNAIL and the storage cavity takes the form³⁷

$$H/\hbar = H_{\text{KCQ}}/\hbar - \chi_{ab}a^\dagger ab^\dagger b + g_{\text{BS}}a^\dagger b + g_{\text{BS}}^*ab^\dagger, \quad (2)$$

where $\chi_{ab}a^\dagger ab^\dagger b$ is the parasitic cross-Kerr interaction and $g_{\text{BS}}a^\dagger b + g_{\text{BS}}^*ab^\dagger$ is the beamsplitter interaction. Assuming that the KCQ remains in its degenerate ground state manifold, we project onto the cat-qubit subspace with the projector $\mathcal{P}_{\mathcal{C}} = |\mathcal{C}_\alpha^+\rangle\langle\mathcal{C}_\alpha^+| + |\mathcal{C}_\alpha^-\rangle\langle\mathcal{C}_\alpha^-|$ and obtain

$$\begin{aligned} H_{\text{int}}/\hbar = & g_{\text{BS}}\alpha\left((b^\dagger + b)\sigma_z + ie^{-2\alpha^2}(b^\dagger - b)\sigma_y\right) \\ & - \chi_{ab}\alpha^2b^\dagger b\left(1 - 2e^{-2\alpha^2}\sigma_x\right). \end{aligned} \quad (3)$$

See Supplementary Information Section I for more details on this derivation. In general, the cross-Kerr interaction will lead to dephasing of the storage cavity due to photon shot noise in the SNAIL. As we increase α , however, the entangling term proportional to $b^\dagger b\sigma_x$ becomes exponentially suppressed such that the cross-Kerr interaction simplifies into a Stark shift, thereby preventing KCQ-cavity entanglement during idling time. This feature is crucial for engineering an ancilla with a large on-off ratio of cavity control, where the interaction between the ancilla and the cavity is only activated via a driven parametric process.

In the limit of $\alpha \gg 1$, Eq. (3) simplifies to a conditional displacement interaction and a Stark shift given by

$$H_{\text{int}}/\hbar \approx g_{\text{BS}}\alpha(b^\dagger + b)\sigma_z - \chi_{ab}\alpha^2b^\dagger b. \quad (4)$$

By tracking this Stark shift and evolving for time $t = \beta/(2g_{\text{BS}}\alpha)$, we realize the conditional displacement unitary $\text{CD}(\beta) = D(-\beta/2) - \alpha|-\alpha\rangle\langle-\alpha| + D(+\beta/2)|+\alpha\rangle\langle+\alpha|$, where $D(\beta) = \exp(\beta b^\dagger - \beta^* b)$ is the displacement operator and the conditional displacement rate $g_{\text{CD}} = 2g_{\text{BS}}\alpha$ is enhanced by having more photons in the KCQ. Together with the single qubit gates on the KCQ, this conditional displacement gate enables universal control of the system³⁸.

A schematic of our experimental setup is shown in Fig. 1b. It consists of a sapphire chip sandwiched between two 3D superconducting microwave post cavities machined out of high-purity aluminum⁴⁷. On the sapphire substrate we fabricated tantalum-based superconducting circuits^{48,49}, which capacitively couple to the 3D

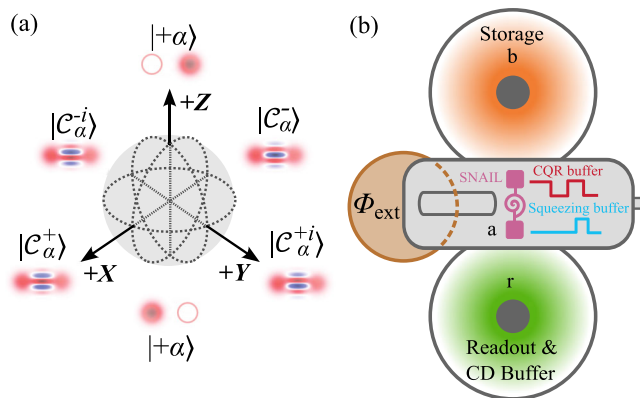


Fig. 1 | Kerr-cat qubit Bloch sphere and experimental schematic. **a** Bloch sphere of the Kerr-cat qubit (KCQ). **b** Schematic of the experimental setup for coupling a KCQ (realized in a SNAIL mode, pink) to a high-Q storage cavity. The active modes of the system are the storage mode, the readout mode and the SNAIL (Superconducting Nonlinear Asymmetric Inductive eElement)^{43–45} mode, whereas the buffer modes are used to facilitate parametric drives to the SNAIL, in particular the CQR (cat qubit readout) drive, the CD (conditional displacement) drive and the squeezing drive.

cavities via waveguide tunnels. The active modes of our system are the on-chip SNAIL mode ($\omega_a = 2\pi \times 4.00$ GHz), the fundamental mode of the 3D storage cavity ($\omega_b = 2\pi \times 7.02$ GHz) and the first harmonic of the 3D readout cavity ($\omega_r = 2\pi \times 9.36$ GHz). The remaining modes in our system are buffers for delivering parametric drives to the SNAIL; they are essentially Purcell filters, designed to be detuned from the desired drive frequency by about 50 MHz⁵⁰. These buffer modes are the on-chip stripline resonator for delivering the CQR drive ($\omega_{\text{CQR}} = \omega_r - \omega_s/2 = 2\pi \times 5.36$ GHz), the on-chip stripline resonator for delivering the squeezing drive ($\omega_s = 2\omega_a = 2\pi \times 8.00$ GHz), and the fundamental frequency of the 3D readout cavity used for delivering the CD drive ($\omega_{\text{CD}} = \omega_b - \omega_s/2 = 2\pi \times 3.02$ GHz). Magnetic flux is delivered to the SNAIL with a solenoid (consisting of a copper coil wound with superconducting NbTi wire) and an on-chip superconducting flux transformer⁵⁰. For all of our experiments we operate the SNAIL at a flux-bias point of $\Phi_{\text{ext}} = 0.32\Phi_0$, where the SNAIL circuit has appreciable g_3 and g_4 values⁵¹, and the frequency conditions of the various parametric processes are reasonably close to their buffer modes. See Supplementary Information Section II for more detail on the experimental apparatus and the fabrication process.

With this experimental setup, we have demonstrated KCQ gates and readout following ref. 37 (see Supplementary Information Section IV), as well as characterized both the bare SNAIL lifetimes and the KCQ lifetimes. In particular, the SNAIL has an energy relaxation lifetime $T_{1,a} = 16.0 \pm 0.4$ μ s and a Ramsey coherence lifetime $T_{2,a} = 7.2 \pm 0.1$ μ s. For our standard cat size of $\alpha^2 = 4$ that is used throughout this manuscript, the KCQ has a coherent state lifetime $T_z = 147 \pm 4$ μ s and a cat state lifetime $T_{X,Y} = 2.32 \pm 0.04$ μ s. The $\sigma_x(\pi/2)$ rotation, realized by free evolution of the SNAIL under its Kerr nonlinearity, takes $T_K = 272$ ns corresponding to $K/2\pi = 0.93 \pm 0.03$ MHz. Additional information on our system characterization can be found in Section IV of the Supplementary Information.

To demonstrate a coherent conditional displacement interaction between the storage cavity and the KCQ, we perform characteristic function (CF) tomography on the storage cavity using the KCQ^{38,40,41}. The characteristic function is defined as $C(\beta) = \langle D(\beta) \rangle$, and it can be measured by initializing the KCQ in the $|C_\alpha^{\pm i}\rangle$ state, performing $CD(\beta)$, and measuring the KCQ along its X and Y axes. The principle of this measurement is that when implementing a conditional displacement $CD(\beta)$ between the KCQ and the storage cavity, the KCQ rotates about its z-axis by an amount that encodes the phase of the displacement

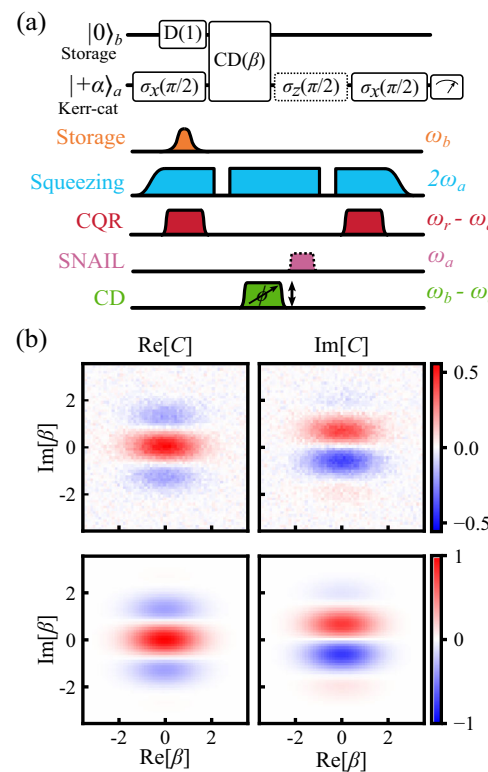


Fig. 2 | Cavity state tomography with a Kerr-cat qubit. **a** Gate sequence (upper) and pulse sequence (lower) for performing characteristic function tomography of a coherent state of amplitude 1 in the storage cavity with the KCQ. The pulse lengths are not to scale. **b** Experimental (upper) and theoretical (lower) characteristic function tomography of a coherent state with amplitude 1 in the cavity, demonstrating the coherence of the conditional displacement interaction. Note that the characteristic function of a coherent state $|\eta\rangle$ is given by $C(\beta) = \exp(-|\beta|^2/2) \exp(\beta\eta^* - \eta\beta^*)$, where the second exponential term provides the interference fringes observed in the plot. This expression originates from the geometric phase associated with displacements according to $D(\eta)D(\beta) = \exp(2iA)D(\beta)D(\eta)$ with $A = \text{Im}[\eta\beta^*]$.

operator, such that $\langle D(\beta) \rangle = \pm \langle \sigma_y \rangle \mp i\langle \sigma_x \rangle$, where the signs are determined by the choice of initial state.

To perform CF tomography, we follow the pulse sequence depicted in Fig. 2a. First, we prepare a coherent state of amplitude 1 in the storage cavity by driving the cavity resonantly with a Gaussian pulse (duration 480 ns). At the same time, we prepare a parity-less cat state $|C_\alpha^{\pm i}\rangle$ in the KCQ by ramping up the squeezing drive (duration 2 μ s), projecting into a coherent state with a CQR measurement (duration 2.5 μ s), and performing a $\sigma_x(\pi/2)$ gate (duration 272 ns). Next, we implement a conditional displacement gate $CD(\beta)$ with varying amplitude and phase of β (duration 348 ns, corresponding to the rate $g_{\text{CD}}/2\pi = 6.18 \pm 0.06$ MHz). Finally, we repeat the experiment multiple times, measuring the KCQ along the X and Y axes to determine the real and imaginary parts of the characteristic function; to measure along the Y axis we perform a $\sigma_x(\pi/2)$ gate followed by a CQR measurement (duration 2.5 μ s), whereas to measure along the X axis we prepend this sequence with a $\sigma_z(\pi/2)$ gate (duration 80 ns). The results of this measurement are shown in Fig. 2b. The contrast of the CF tomography is limited by photon-loss errors in the SNAIL during the $\sigma_x(\pi/2)$ rotation. Aside from reduced contrast, we find excellent agreement between our experimental results and theoretical predictions. Furthermore, the fact that we are able to imprint the phase associated with the displacement operator onto the equator of the KCQ demonstrates the coherence of the CD gate, which we are able to observe due to the CD rate g_{CD} being faster than all decoherence rates in our system.

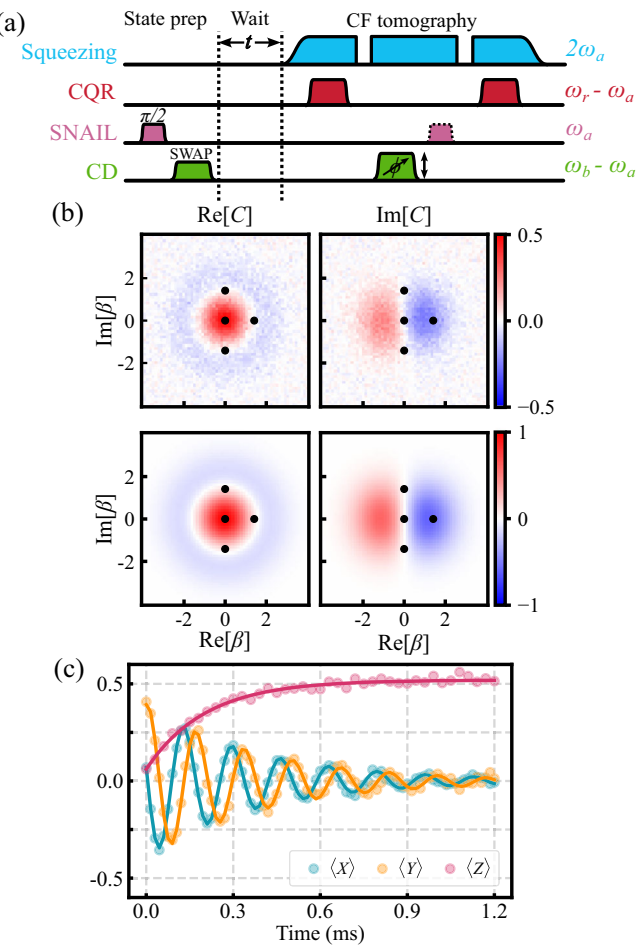


Fig. 3 | Cavity lifetime measurement with a Kerr-cat qubit. a Pulse sequence for storage cavity lifetime measurements. We prepare a $(|0\rangle + i|1\rangle)/\sqrt{2}$ state in the storage, wait a variable time t , and perform characteristic function tomography at specific values of β to reconstruct the expectation values of the Pauli operators of the storage Fock qubit (spanned by the $|0\rangle$ and $|1\rangle$ states). **b** Measured (upper) and predicted (lower) characteristic function (CF) of the $(|0\rangle + i|1\rangle)/\sqrt{2}$ state prepared in the storage cavity. The four points in the plot are the values of β at which we sample the CF in order to measure the Pauli expectation values of the Fock qubit in the storage cavity. **c** Evolution of the expectation values $\langle X \rangle$, $\langle Y \rangle$ and $\langle Z \rangle$ of the storage Fock qubit as a function of time, from which we can determine $T_1 = 204 \pm 9 \mu\text{s}$ and $T_2 = 381 \pm 8 \mu\text{s}$. The fits are displayed in solid lines.

Combined with single-qubit gates on the KCQ, this CD gate enables universal quantum control of the cavity³⁸.

In order to use this platform for bosonic quantum error correction, we need to demonstrate the ability to maintain storage coherence while establishing a KCQ in the SNAIL. From Eqs. (3) and (5), we expect the storage dephasing due to SNAIL photon shot noise to be suppressed as we increase α^2 , which we can verify experimentally by measuring the energy relaxation rate and dephasing rate of the storage cavity in the presence of a KCQ with varying size α . As a first step, we develop a method of measuring the storage coherences that is amenable to our experimental setup.

Similar to other approaches^{17,38,40,41,52}, we measure T_1 and T_2 of the storage cavity by restricting the cavity to its Fock-qubit subspace (spanned by $|0\rangle$ and $|1\rangle$), with Pauli operators X , Y , and Z , preparing the state $|+Y\rangle = (|0\rangle + i|1\rangle)/\sqrt{2}$, and measuring $\langle X(t) \rangle$, $\langle Y(t) \rangle$ and $\langle Z(t) \rangle$ while the cavity state decays. Our control sequence for this measurement is shown in Fig. 3a. To prepare the $|+Y\rangle$ state in the storage we first excite the SNAIL to the $(|g\rangle + i|e\rangle)/\sqrt{2}$ state with a square pulse of duration

$1.1 \mu\text{s}$, after which we drive a beamsplitter interaction at $\omega_b - \omega_a$ for $1.5 \mu\text{s}$ to swap the SNAIL state into the storage cavity. The square pulse of duration $1.1 \mu\text{s}$ is designed such that its frequency distribution is a sinc function with a notch at the anharmonicity of the SNAIL, thereby minimizing leakage of the SNAIL to its $|f\rangle$ state. To measure $\langle X(t) \rangle$, $\langle Y(t) \rangle$ and $\langle Z(t) \rangle$ we use a method adapted from ref. 52: assuming we remain in the Fock-qubit subspace of the storage cavity, these Pauli expectation values can be determined by measuring the characteristic function $\mathcal{C}(\beta)$ at the four points $\beta = 0, \sqrt{2}, \sqrt{2}i, -\sqrt{2}i$. See Supplementary Information Section VII for more detailed information.

The experimentally measured $\langle X(t) \rangle$, $\langle Y(t) \rangle$ and $\langle Z(t) \rangle$ are shown in Fig. 3c, where the decay of $\langle Z(t) \rangle$ tells us $T_1 = 204 \pm 9 \mu\text{s}$ and the ring-downs of $\langle X(t) \rangle$ and $\langle Y(t) \rangle$ tell us $T_2 = 381 \pm 8 \mu\text{s}$, corresponding to a pure dephasing rate $\Gamma_\phi = (5.7 \pm 2.8 \text{ ms})^{-1}$. Bare microwave cavities have minimal intrinsic dephasing^{25,49,53–55}, so we expect this dephasing to be dominated by heating in the SNAIL coupling to the storage cavity via the cross-Kerr interaction, which we verify experimentally by measuring the thermal population of the SNAIL. Owing to the low contrast of SNAIL dispersive readout, we cannot carry out this measurement directly (see Supplementary Information Section III for details). To get around this limitation, we map the thermal population of the SNAIL into the storage by swapping their states (via a beam-splitter interaction, see Supplementary Information Section X for details) after the system reaches thermal equilibrium, and then perform CF tomography on the storage. The width σ_{th} of the resulting Gaussian is related to the thermal population in the storage according to $\sigma_{\text{th}} = 1/\sqrt{2n_{\text{th}} + 1}$. We find $n_{\text{th}} = 2.8 \pm 0.5\%$, corresponding to an induced dephasing rate⁵⁶ of $\Gamma_\phi = (7.3 \pm 1.3 \text{ ms})^{-1}$, which agrees with our direct measurement of the storage dephasing rate. It is important to note that this method assumes that the storage cavity at 7 GHz has a much lower thermal population than the SNAIL at 4 GHz, but the fact that these two independent measurements of the storage dephasing rate agree with one another is consistent with this assumption.

With this technique for characterizing the storage lifetimes, we can investigate the effect of the second term of Eq. (3),

$$H_\chi/h = -\chi_{ab}\alpha^2 b^\dagger b \left(1 - 2e^{-2\alpha^2}\sigma_x\right), \quad (5)$$

which arises from the cross-Kerr interaction between the SNAIL and the storage cavity with $\chi_{ab}/2\pi = 2.91 \pm 0.03 \text{ kHz}$ (see Supplementary Information Section VIII for our cross-Kerr characterization details). The first term is a Stark shift of the storage due to photons in the KCQ, which can be tracked in software. The second term corresponds to a residual cross-Kerr interaction between the KCQ and the storage, where the strength of the interaction peaks at $\alpha^2 = 1/2$ and is then exponentially suppressed with the number of photons α^2 in the KCQ. Under this interaction, parity flips in the KCQ (due to photon shot noise in the SNAIL) induce dephasing in the storage, just as SNAIL heating gave rise to storage dephasing in the previous measurement. When we increase the size of the KCQ, this dephasing is exponentially suppressed, keeping the KCQ disentangled from the storage and preserving the coherence of the storage cavity. To examine this effect experimentally, we modify our previous measurement by stabilizing a KCQ with varying size α while we idle the storage cavity (pulse sequence depicted in Fig. 4a). Then we measure $\langle X(t) \rangle$, $\langle Y(t) \rangle$ and $\langle Z(t) \rangle$ of the storage cavity using the method discussed above and shown in Fig. 3. The result of this measurement is shown in Fig. 4b. As α increases from zero, the cavity experiences more dephasing, causing T_2 to decrease. Upon reaching half a photon in the KCQ, we observe maximum storage dephasing and a subsequent revival of storage T_2 as α increases, indicating suppression of photon shot noise as predicted in Eq. (5). However, the revival does not continue all the way to $T_2 = 2T_1$, which corresponds to the region colored in light green in Fig. 4(b). This

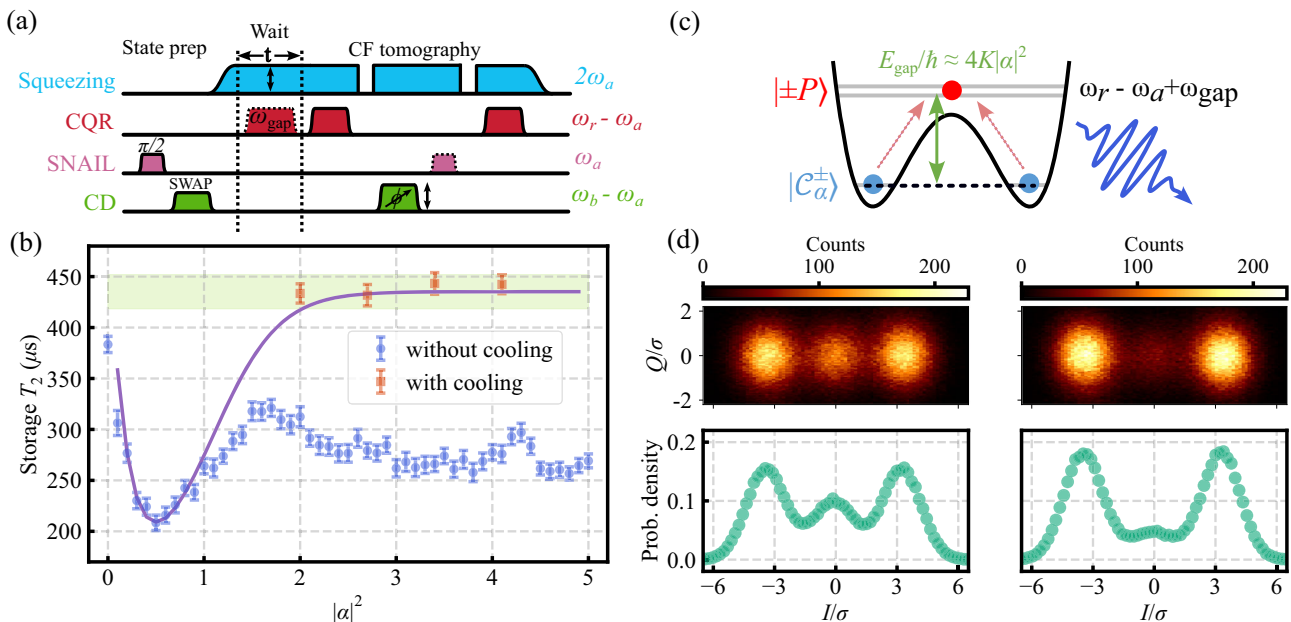


Fig. 4 | Cavity lifetime in the presence of a Kerr-cat qubit. **a** Pulse sequence measuring storage cavity T_1 and T_2 in the presence of a KCQ. **b** Measurement results for storage dephasing in the presence of a KCQ with varying size α . The blue circles are measured without cooling the KCQ, the orange squares are measured with active cooling via frequency-selective dissipation (FSD), and the error bars are one standard deviation. The purple line serves as a guide to the eye for our results, assuming a pure dephasing rate of the storage proportional to χ_{eff}^2 according to Fermi's golden rule, where $\chi_{\text{eff}}(\alpha) = 2\alpha^2\chi_{ab} \exp(-2\alpha^2)$ is the effective cross-Kerr

strength. The green region is our one standard deviation confidence interval of the storage T_1 we obtain from these measurements, taken over a one-month period, corresponding to $435 \pm 17 \mu s$. **c** Schematic representation of the metapotential and the lowest-lying energy levels of a KCQ with $n_{\text{cat}} = 4$. We dissipate the excited state population of the KCQ into the readout cavity via a three-wave mixing process. **(d)** CQR/I/Q signal histograms (upper panel) and their marginals along the I quadrature (lower panel) of the KCQ with artificially-induced heating before (left) and after (right) FSD. See Supplementary Information Section XII for more information.

additional channel of dephasing in the storage cavity is due to heating in the KCQ, as we will demonstrate.

To illustrate the physics of the storage dephasing, we consider a KCQ with $\alpha = 2$, the potential energy and eigenstates of which are shown in Fig. 4(c). The states at the minima are the degenerate ground states of the metapotential, forming the computational subspace of the KCQ, whereas the first excited states are non-degenerate excited states outside of the wells. These excited states have different average photon number than the ground states, and therefore cause different Stark-shifts of the storage cavity (see Supplementary Information Section I for details). Without heating, the KCQ would stay in the degenerate ground states and remain disentangled from the storage cavity. With heating, indicated by the dotted red arrows, the KCQ would transition from the ground states to the excited states, dephasing the storage cavity.

One way to mitigate this dephasing is through a frequency-selective dissipation (FSD) of the excited state population of the KCQ³¹. The idea is to dissipate excited state population through a lossy mode without affecting the ground state manifold. Whereas ref. 31 proposed using filter modes that are on resonance with the energy gap of the KCQ, here we use the three-wave mixing capability of our SQUID to hybridize the first excited state manifold of the KCQ with the readout cavity. This method is convenient to perform in our setup, as the beamsplitter interaction required by this process is our built-in CQR interaction with a detuning, giving us $\omega_{\text{FSD}} = \omega_r - \omega_s/2 + \omega_{\text{gap}}$. We calibrate the energy gap $\omega_{\text{gap}}/2\pi = 12.5$ MHz at $\alpha = 2$ by performing spectroscopy on the excited states of the KCQ (see Supplementary Information Section IV D for details). To calibrate the amplitude of the FSD drive, we need a way to measure the population of the excited state manifold. Due to the fact that the CQR drive does not displace the readout cavity when the KCQ is in an excited state outside of the wells, the center blob in the I/Q plane of the CQR signal correlates with the total excited state population (see

Supplementary Information section XII A for more details). We set the FSD amplitude to the value that minimizes this signal, as is shown in Fig. 4(d).

With the FSD, we can experimentally verify that the storage dephasing is due to KCQ heating. To do so, we repeat the previous measurement shown in Fig. 3 at $\alpha^2 = 2.0, 2.7, 3.4$ and 4.1 , except now we apply the FSD drive to the KCQ during the storage idling time. As shown in Fig. 4b, the active cooling on the KCQ improves T_2 of the storage cavity to a level consistent with zero dephasing, up to the precision of our measurement, while T_1 of the storage cavity is unaffected. Based on the error bars of these measurements of T_1 and T_2 , we estimate the upper bound of the residual dephasing rate in the storage cavity to be $(27 \text{ ms})^{-1}$.

In addition to verifying the origin of the storage dephasing, this result validates the interaction Hamiltonian (Eq. (3)) between the storage and the KCQ: for sufficiently large cats, the storage and the KCQ do not entangle, provided that the KCQ stays in its computational manifold. Furthermore, the fact that the two systems do not entangle unless we are actively driving their interaction demonstrates a high on-off ratio of control. To quantify this ratio, we assume there exists a residual interaction $\chi_{\text{res}} b^\dagger b \sigma_x$ between the storage cavity and the KCQ, giving rise to residual dephasing consistent with our measurement precision. Based on our bound for the residual dephasing rate, we can bound $\chi_{\text{res}}/2\pi < 1$ kHz, yielding a bound on the on-off control ratio of $g_{\text{CD}}/\chi_{\text{res}} > 6000$ (see Supplementary Information Section IX for the corresponding analysis). We emphasize that these are conservative bounds limited by our measurement precision, and based on the assumption that FSD removes all the excited state population.

Discussion

We note that the origin of the KCQ heating is a subject of ongoing research. In addition to the cavity dephasing that we observe, this

heating causes the staircase-like pattern in the coherent state lifetime of the KCQ that is observed as the squeezing drive strength is increased^{28–30,36} (also see Supplementary Fig. 8(f)). Although we understand the qualitative features of this staircase, we do not yet have a quantitative understanding of the KCQ lifetimes in terms of the underlying physical error rates of the SNAIL.

In summary, we have experimentally realized a coherent parametrically-driven CD gate between a KCQ and a high-quality-factor storage cavity that, combined with single-qubit KCQ gates, enables universal quantum control of the cavity³⁸. By actively cooling the KCQ we were able to prevent the two systems from entangling during idling time, thereby demonstrating a high on-off ratio of control. The operations we have demonstrated constitute all the necessary ingredients for stabilizing Gottesman-Kitaev-Preskill codewords in the storage cavity^{11,39,40}, paving the way towards fault-tolerant quantum error correction of this code²⁶. To achieve this, we need to implement a higher quality $\sigma_x(\pi/2)$ Kerr-cat rotation, for instance by improving the coherence of the SNAIL or by using alternative strategies for realizing this rotation^{27,29,57}. In addition to performing fault-tolerant syndrome measurements of bosonic codes, the experimental platform we developed for coupling a Kerr-cat to a cavity could be useful for realizing error-transparent gates in hybrid discrete/continuous variable systems⁵⁸. Finally, our understanding of the Kerr-cat-induced cavity dephasing and its mitigation with active cooling will be important for other experiments in which Kerr-cats are coherently coupled to other systems^{59,60}.

Data availability

The data that support the findings of this study are available on Zenodo at <https://doi.org/10.5281/zenodo.15361822>.

Code availability

The code used to analyze the experimental data is available on Zenodo at <https://doi.org/10.5281/zenodo.15361822>.

References

- Shor, P. Fault-tolerant quantum computation. *Proceedings of 37th Conference on Foundations of Computer Science*, 56 (1996).
- Knill, E., Laflamme, R. & Zurek, W. H. Resilient quantum computation. *Science* **279**, 342 (1998).
- Aharonov, D. & Ben-Or, M. Fault-tolerant quantum computation with constant error rate. *SIAM J. Comput.* **38**, 1207 (2008).
- Kitaev, A. Y. Fault-tolerant quantum computation by anyons. *Ann. Phys.* **303**, 2 (2003).
- Fowler, A. G., Mariantoni, M., Martinis, J. M. & Cleland, A. N. Fault-tolerant quantum computation by anyons. *Phys. Rev. A - , Mol., Optical Phys.* **86**, 032324 (2012).
- Kivlichan, I. D. et al. Improved fault-tolerant quantum simulation of condensed-phase correlated electrons via trotterization. *Quantum* **4**, 296 (2020).
- Lee, J. et al. Even more efficient quantum computations of chemistry through tensor hypercontraction. *PRX Quantum* **2**, 030305 (2021).
- Gottesman, D. Fault-Tolerant quantum computation with constant overhead. *Quantum Inf. Comput.* **14**, 1338 (2014).
- Breuckmann, N. P. & Eberhardt, J. N. Quantum low-density parity-check codes. *PRX Quantum* **2**, 040101 (2021).
- Chuang, I. L., Leung, D. W. & Yamamoto, Y. Bosonic quantum codes for amplitude damping. *Phys. Rev. A* **56**, 1114 (1997).
- Gottesman, D., Kitaev, A. & Preskill, J. Encoding a qubit in an oscillator. *Phys. Rev. A* **64**, <https://doi.org/10.1103/PhysRevA.64.012310> (2001).
- Michael, M. H. et al. New class of quantum error-correcting codes for a bosonic mode. *Phys. Rev. X* **6**, 031006 (2016).
- Mirrahimi, M. et al. Dynamically protected cat-qubits: A new paradigm for universal quantum computation. *N. J. Phys.* **16**, 045014 (2014).
- Joshi, A., Noh, K. & Gao, Y. Y. Quantum information processing with bosonic qubits in circuit QED. *Quantum Sci. Technol.* **6**, 033001 (2021).
- Cai, W., Ma, Y., Wang, W., Zou, C. L. & Sun, L. Bosonic quantum error correction codes in superconducting quantum circuits. *Fundamental Res.* **1**, 50 (2021).
- Ofeq, N. et al. Extending the lifetime of a quantum bit with error correction in superconducting circuits. *Nature* **536**, 441 (2016).
- Sivak, V. V. et al. Real-time quantum error correction beyond break-even. *Nature* **616**, 50 (2023).
- Ni, Z. et al. Beating the break-even point with a discrete-variable-encoded logical qubit. *Nat. 2023 616:7955* **616**, 56 (2023).
- Brock, B. L. et al. Quantum error correction of qudits beyond break-even. *Nature* **641**, 612–618 (2025).
- Gertler, J. M. et al. Protecting a bosonic qubit with autonomous quantum error correction. *Nat. 2021 590:7845* **590**, 243 (2021).
- de Neeve, B., Nguyen, T. L., Behrle, T. & Home, J. P. Error correction of a logical grid state qubit by dissipative pumping. *Nat. Phys.* **2022 18:3** **18**, 296 (2022).
- Lachance-Quirion, D. et al. Autonomous Quantum Error Correction of Gottesman-Kitaev-Preskill States. *Phys. Rev. Lett.* **132**, 150607 (2024).
- Blais, A., Huang, R.-S., Wallraff, A., Girvin, S. M. & Schoelkopf, R. J. Cavity quantum electrodynamics for superconducting electrical circuits: An architecture for quantum computation. *Phys. Rev. A* **69**, 062320 (2004).
- Blais, A., Grimsmo, A. L., Girvin, S. M. & Wallraff, A. Circuit quantum electrodynamics. *Rev. Mod. Phys.* **93**, 025005 (2021).
- Rosenblum, S. et al. Fault-tolerant detection of a quantum error. *Science* **361**, 266 (2018).
- Puri, S. et al. Stabilized cat in a driven nonlinear cavity: A fault-tolerant error syndrome detector. *Phys. Rev. X* **9**, 041009 (2019).
- Puri, S., Boutin, S. & Blais, A. Engineering the quantum states of light in a Kerr-nonlinear resonator by two-photon driving. *npj Quantum Inf.* **3**, 1 (2017).
- Frattini, N. E. et al. Observation of pairwise level degeneracies and the quantum regime of the Arrhenius law in a double-well parametric oscillator. *Phys. Rev. X* **14**, 031040 (2024).
- Hajr, A. et al. High-coherence Kerr-Cat qubit in 2D architecture. *Phys. Rev. X* **14**, 041049 (2024).
- Qing, B. et al. Benchmarking single-qubit gates on a noise-biased qubit beyond the fault-tolerant threshold (2024), arXiv:2411.04442 [quant-ph].
- Puterman, H. et al. Stabilizing a Bosonic Qubit Using Colored Dissipation. *Phys. Rev. Lett.* **128**, 110502 (2022).
- Bhandari, B. et al. Symmetrically threaded squids as next generation Kerr-cat qubits. arXiv:2405.11375 (2024).
- Venkatraman, J., Cortiñas, R. G., Frattini, N. E., Xiao, X. & Devoret, M. H. A driven Kerr oscillator with two-fold degeneracies for qubit protection. *Proc. Natl. Acad. Sci. USA* **121**, <https://doi.org/10.1073/PNAS.2311241121> (2024).
- Gravina, L., Minganti, F. & Savona, V. Critical Schrödinger cat qubit. *PRX Quantum* **4**, 020337 (2023).
- Ruiz, D., Gautier, R., Guillaud, J. & Mirrahimi, M. Two-photon driven Kerr quantum oscillator with multiple spectral degeneracies. *Phys. Rev. A* **107**, 042407 (2023).
- Su, Q., Cortiñas, R. G., Venkatraman, J. & Puri, S. Unraveling the switching dynamics in a quantum double-well potential. arXiv:2501.00209 (2024).
- Grimm, A. et al. Stabilization and operation of a Kerr-cat qubit. *Nature* **584**, 205 (2020).
- Eickbusch, A. et al. Fast universal control of an oscillator with weak dispersive coupling to a qubit. *Nat. Phys.* **18**, 1464 (2022).
- Terhal, B. M. & Weigand, D. Encoding a qubit into a cavity mode in circuit QED using phase estimation. *Phys. Rev. A* **93**, 012315 (2016).

40. Campagne-Ibarcq, P. et al. Quantum error correction of a qubit encoded in grid states of an oscillator. *Nature* **584**, 368 (2020).
41. Flühmann, C. & Home, J. P. Direct Characteristic-Function Tomography of Quantum States of the Trapped-Ion Motional Oscillator. *Phys. Rev. Lett.* **125**, 043602 (2020).
42. Dykman, M. *Fluctuating Nonlinear Oscillators: From Nanomechanics to Quantum Superconducting Circuits* (OUP Oxford, 2012).
43. Frattini, N. E. et al. 3-wave mixing Josephson dipole element. *Appl. Phys. Lett.* **110**, 222603 (2017).
44. Sivak, V. V. et al. Kerr-Free Three-Wave Mixing in Superconducting Quantum Circuits. *Phys. Rev. Appl.* **10**, 54060 (2019).
45. Frattini, N. E. *Three-Wave Mixing in Superconducting Circuits: Stabilizing Cats with SNAILS*, Phd thesis, Yale University (2021).
46. Kirchmair, G. et al. Observation of quantum state collapse and revival due to the single-photon Kerr effect. *Nature* **495**, 205 (2013).
47. Reagor, M. et al. Reaching 10 ms single photon lifetimes for superconducting aluminum cavities. *Appl. Phys. Lett.* **102**, 192604 (2013).
48. Place, A. P. et al. New material platform for superconducting transmon qubits with coherence times exceeding 0.3 milliseconds. *Nat. Commun.* **12**, 1 (2021).
49. Ganjam, S. et al. Surpassing millisecond coherence in on chip superconducting quantum memories by optimizing materials and circuit design. *Nat. Commun.* **15**, 1 (2024).
50. Chapman, B. J. et al. High-on-off-ratio beam-splitter interaction for gates on bosonically encoded qubits. *PRX Quantum* **4**, 020355 (2023).
51. Chávez-Carlos, J. et al. Driving superconducting qubits into chaos. *Quantum Sci. Technol.* **10**, 015039 (2025).
52. Koottandavida, A. et al. Erasure detection of a dual-rail qubit encoded in a double-post superconducting cavity. *Phys. Rev. Lett.* **132**, 180601 (2024).
53. Reagor, M. et al. Quantum memory with millisecond coherence in circuit QED. *Phys. Rev. B* **94**, 014506 (2016).
54. Milul, O. et al. Superconducting cavity qubit with tens of milliseconds single-photon coherence time. *PRX Quantum* **4**, 030336 (2023).
55. Chakram, S. et al. Seamless high-Q microwave cavities for multimode circuit quantum electrodynamics. *Phys. Rev. Lett.* **127**, 107701 (2021).
56. Clerk, A. A. & Utami, D. W. Using a qubit to measure photon-number statistics of a driven thermal oscillator. *Phys. Rev. A - Mol. Opt. Phys.* **75**, 042302 (2007).
57. Goto, H. Universal quantum computation with a nonlinear oscillator network. *Phys. Rev. A* **93**, 050301 (2016).
58. Pietikäinen, I., Černotík, O., Puri, S., Filip, R. & Girvin, S. M. Controlled beam splitter gate transparent to dominant ancilla errors. *Quantum Sci. Technol.* **7**, 035025 (2022).
59. Iyama, D. et al. Observation and manipulation of quantum interference in a superconducting Kerr parametric oscillator. *Nat. Commun.* **15**, 1 (2024).
60. Hoshi, D. et al. Entangling Schrödinger's cat states by bridging discrete-and continuous-variable encoding. *Nat. Commun.* **16**, 1309 (2025).

Acknowledgements

We thank S. M. Girvin, Y. Lu, S. Puri, A. P. Read, M. Schäfer, S. Singh, V. V. Sivak, Q. Su, J. Venkatraman and X. Xu for helpful discussions. We are grateful to J. Curtis for technical assistance and I. Tsoutsios for device fabrication assistance. Finally, we thank Y. Sun, K. Woods, L. McCabe and M. Rooks for their assistance and guidance in the device fabrication processes. This research was sponsored by the Army Research Office (ARO) under grant nos. W911NF-23-1-0051, by the Air Force Office of Scientific Research (AFOSR) under grant FA9550-19-1-0399 and by the U.S. Department of Energy (DoE), Office of Science, National Quantum Information Science Research Centers, Co-design Center for Quantum Advantage (C2QA) under contract number DE-SC0012704. The views and

conclusions contained in this document are those of the authors and should not be interpreted as representing the official policies, either expressed or implied, of the ARO, AFOSR, DoE or the US Government. The US Government is authorized to reproduce and distribute reprints for Government purposes notwithstanding any copyright notation herein. Fabrication facilities use was supported by the Yale Institute for Nanoscience and Quantum Engineering (YINQE) and the Yale SEAS Cleanroom.

Author contributions

A.Z.D., B.L.B. and A.E. designed the experimental setup. A.Z.D. fabricated the device, with assistance from S.G. and L.F. S.J.d.G. and B.J.C. contributed to the 3D cavity design. A.Z.D. and B.L.B. built the microwave control electronics. V.R.J. designed and fabricated the SNAIL parametric amplifier. A.Z.D. performed the measurements with supervision from B.L.B. A.E., A.K., N.E.F. and R.G.C. provided valuable help with the measurements. B.L.B. and A.Z.D. developed the method for performing frequency-selective dissipation on the Kerr-cat. B.L.B. and A.K. assisted with data analysis and cryogenic maintenance. R.J.S. supervised the contributions of S.G., S.J.d.G. and B.J.C. M.H.D. supervised the project. A.Z.D., B.L.B. and M.H.D. wrote the manuscript with feedback from all authors.

Competing interests

L.F. and R.J.S. are founders and shareholders of Quantum Circuits Inc. (QCI). M.H.D. has an advisory role at Google Quantum AI. The remaining authors declare no competing interests.

Additional information

Supplementary information The online version contains supplementary material available at <https://doi.org/10.1038/s41467-025-60352-w>.

Correspondence and requests for materials should be addressed to Andy Z. Ding, Benjamin L. Brock or Michel H. Devoret.

Peer review information: *Nature Communications* thanks Luyan Sun, and the other, anonymous, reviewers for their contribution to the peer review of this work. A peer review file is available.

Reprints and permissions information is available at <http://www.nature.com/reprints>

Publisher's note Springer Nature remains neutral with regard to jurisdictional claims in published maps and institutional affiliations.

Open Access This article is licensed under a Creative Commons Attribution-NonCommercial-NoDerivatives 4.0 International License, which permits any non-commercial use, sharing, distribution and reproduction in any medium or format, as long as you give appropriate credit to the original author(s) and the source, provide a link to the Creative Commons licence, and indicate if you modified the licensed material. You do not have permission under this licence to share adapted material derived from this article or parts of it. The images or other third party material in this article are included in the article's Creative Commons licence, unless indicated otherwise in a credit line to the material. If material is not included in the article's Creative Commons licence and your intended use is not permitted by statutory regulation or exceeds the permitted use, you will need to obtain permission directly from the copyright holder. To view a copy of this licence, visit <http://creativecommons.org/licenses/by-nc-nd/4.0/>.

© The Author(s) 2025